Available online at www.sciencedirect.com

ScienceDirect

ELSEVIER

Ocean Modelling 15 (2006) 218–235

Ocean Modelling

www.elsevier.com/locate/ocemod

Pacific tropical–extratropical thermocline water mass exchanges in the NCAR Coupled Climate System Model v.3

Amy Solomon [a,*], Ilana Wainer [b]

[a] *NOAA/ESRL/PSD/CIRES-Climate Diagnostics Center, R/PSDI, 325 Broadway Boulder, CO 80305, United States*
[b] *Department of Physical Oceanography, University of São Paulo, São Paulo, Brazil*

Received 7 June 2005; received in revised form 23 March 2006; accepted 5 April 2006
Available online 26 May 2006

Abstract

In this study we document how model biases in extratropical surface wind and precipitation, due to ocean–atmosphere coupling, are communicated to the equatorial Pacific thermocline through Pacific Subtropical Cell (STC) pathways. We compare the simulation of climate mean Pacific Subtropical Cells (STCs) in the NCAR Community Climate System Model version 3 (CCSM3) to observations and to an uncoupled ocean simulation (the ocean component of the CCSM3 forced by observed wind stress and surface fluxes). We use two versions of the CCSM3 with atmospheric resolution of 2.8° (T42) and 1.4° (T85) to investigate whether the climate mean STCs are sensitive to the resolution of the atmospheric model.

Since STCs provide water that maintains the equatorial thermocline, we first document biases in equatorial temperature and salinity fields. We then investigate to what extent these biases are due to the simulation of extratropical–tropical water mass exchanges in the coupled models. We demonstrate that the coupled models' cold and fresh bias in the equatorial thermocline is due to the subduction of significantly fresher and colder water in the South Pacific. This freshening is due to too much precipitation in the South Pacific Convergence Zone. Lagrangian trajectories of water that flows to the equatorial thermocline are calculated to demonstrate that the anomalously large potential vorticity barriers in the coupled simulations in both the North and South Pacific prevent water in the lower thermocline from reaching the equator. The equatorial thermocline is shown to be primarily maintained by water that subducts in the subtropical South Pacific in both the coupled and uncoupled simulations. It is shown that the zonally integrated transport convergence at the equator in the subsurface branch of the climate mean STCs is well simulated in the uncoupled ocean model. However, coupling reduces the net equatorward pycnocline transport by ~4 Sv at 9°S and ~1 Sv at 9°N. An increase in the atmospheric resolution from T42 to T85 results in more realistic equatorial trades and off-equatorial convergence zones.

1. Introduction

In the equatorial Pacific, easterly trade winds force an easterly surface flow in the Pacific Ocean with upwelling in the eastern Pacific, poleward Ekman flow to the north and south of the equator and a deep mixed layer in the western Pacific (the Warm Pool), which on the equator extends from the dateline to the western

* Corresponding author. Tel.: +1 303 497 4398.
E-mail address: Amy.Solomon@noaa.gov (A. Solomon).

1463-5003/$ - see front matter
doi:10.1016/j.ocemod.2006.04.003

boundary in the climate mean (Levitus and Boyer (1994), hereafter referred to as the Levitus climatology). This mixed layer is terminated by a sharp vertical temperature gradient, or thermocline, that coincides with an undercurrent that exceeds 50 cm s^{-1} (the Pacific Equatorial Undercurrent or EUC) (e.g., Wyrtki and Kilonsky, 1984). The EUC is primarily maintained by water that subducts in the extratropics and flows equatorward along isopyncals within the permanent thermocline (e.g., Fine et al., 1981, 1987). Water mass properties of this water are essentially determined by wind stress, salt and heat fluxes at the ocean's surface where the water subducts, connecting the extratropical atmosphere with the tropical ocean. This geostrophic equatorward transport within the thermocline that returns to the extratropics through surface Ekman flow defines the Pacific Subtropical Cells (STCs).

In order for a climate model to be used for studies of climate variability it is critical that this flow be adequately simulated. Specifically, the atmospheric forcing of the water mass properties in the region where water subducts in the extratropics, and the pathways that water takes from the extratropics to the tropics. In this paper we investigate these features in the ocean component of the National Center for Atmospheric Research (NCAR) Community Climate System Model version 3 (CCSM3) in an uncoupled integration forced by NCEP winds and fluxes (hereafter referred to as POP3) and two coupled integrations with the atmospheric component of the CCSM3 run on a gaussian gird with approximately 2.8° (T42) and 1.4° (T85) horizontal resolution (hereafter referred to as T42 and T85, respectively).

1.1. Observed STCs

Water that subducts in the extratropics and flows to the EUC within the permanent thermocline forms the equatorward branch of the subtropical cells (STCs; McCreary and Lu, 1994). These shallow (<500 m deep) meridionally overturning cells follow interior or western boundary pathways (depending on where water subducts) to the equatorial thermocline. The STCs provide a pathway by which extratropical atmospheric variability can force tropical variability through the ocean by temperature anomalies, T', that subduct in the extratropics and upwell at the equator (the $\mathbf{V}T'$ mechanism) (Gu and Philander, 1997) or by transport anomalies, V', that change the amount of water that upwells at the equator (the $V'\mathbf{T}$ mechanism) (Kleeman et al., 1999).

In the North Pacific, tracer studies of bomb tritium indicate that surface waters subduct in the eastern subtropics, continue southwestward in the North Equatorial Current, then travel southeastward in the North Equatorial Countercurrent (Fine et al., 1981, 1987). Johnson and McPhaden (1999) used hydrographic data based on individual CTD stations from 1967 through 1998 to estimate that only 5 ± 1 Sv (Sv $\equiv 10^6$ m^3 s^{-1}) reaches the EUC following this interior pathway. In a more recent paper, McPhaden and Zhang (2002) used an updated analysis of hydrographic data from the World Ocean Data Base 1998 augmented with data from archives of the Pacific Marine Environmental Laboratory to estimate a somewhat higher value of 8 ± 3 Sv. By contrast in the South Pacific, Johnson and McPhaden (1999) estimated that 15 ± 1 Sv (compared to 14 ± 3 Sv estimated by McPhaden and Zhang (2002)) flows through a more direct interior pathway to the EUC. The difference in transport along interior pathways in the North and South Pacific is primarily attributed to the potential vorticity (PV) barrier created by the Intertropical Convergence Zone (ITCZ) in the North Pacific, which blocks water from flowing directly to the equator (Liu and Huang, 1998; Lu et al., 1998).

Water that subducts in the central subtropical Pacific tends to flow to the EUC through low-latitude western boundary currents (LLWBC; Liu et al., 1994). Lindstrom et al. (1987) and Butt and Lindstrom (1994) estimated that equivalent transport flows through the North and South Pacific LLWBC to the EUC; 12 Sv in the Mindanao Current and 13 Sv in the New Guinea Coastal Undercurrent (NGCU). Assimilated ocean model data produces similar estimates (Huang and Liu, 1999).

The observed transports discussed in this section are summarized in Table 1.

1.2. Observed sources of equatorial thermocline water

In this subsection we identify subtropical sources of equatorial thermocline water by examining the relationship between subtropical sea surface salinity and the salinity of water that flows to the tropics along STC subsurface pathways. High salinity is seen in both the North and South subtropical Pacific (Fig. 1(a)).

Table 1
Observed pycnocline transports divided into interior and western boundary transports in the North and South Pacific, as well as, net (South Pacific minus North Pacific) interior and western boundary convergence

	NP interior pycnocline transport	NP western boundary transport	SP interior pycnocline transport	SP western boundary transport	Interior pycnocline convergence	Western boundary convergence
BL94		−12 Sv		13 Sv		25 Sv
HL99	−3 Sv	−14 Sv	11 Sv	15 Sv	14 Sv	29 Sv
JM99	−5 ± 1 Sv		15 ± 1 Sv		21 ± 2 Sv	
MZ02	−8 ± 3 Sv		14 ± 3 Sv		22 ± 6 Sv	24 ± 6 Sv

Transport is in units of Sv. Uncertainties in the measurements are included when available. BL94 = Butt and Lindstrom (1994), HL99 = Huang and Liu (1999), JM99 = Johnson and McPhaden (1999), MZ02 = McPhaden and Zhang (2002).

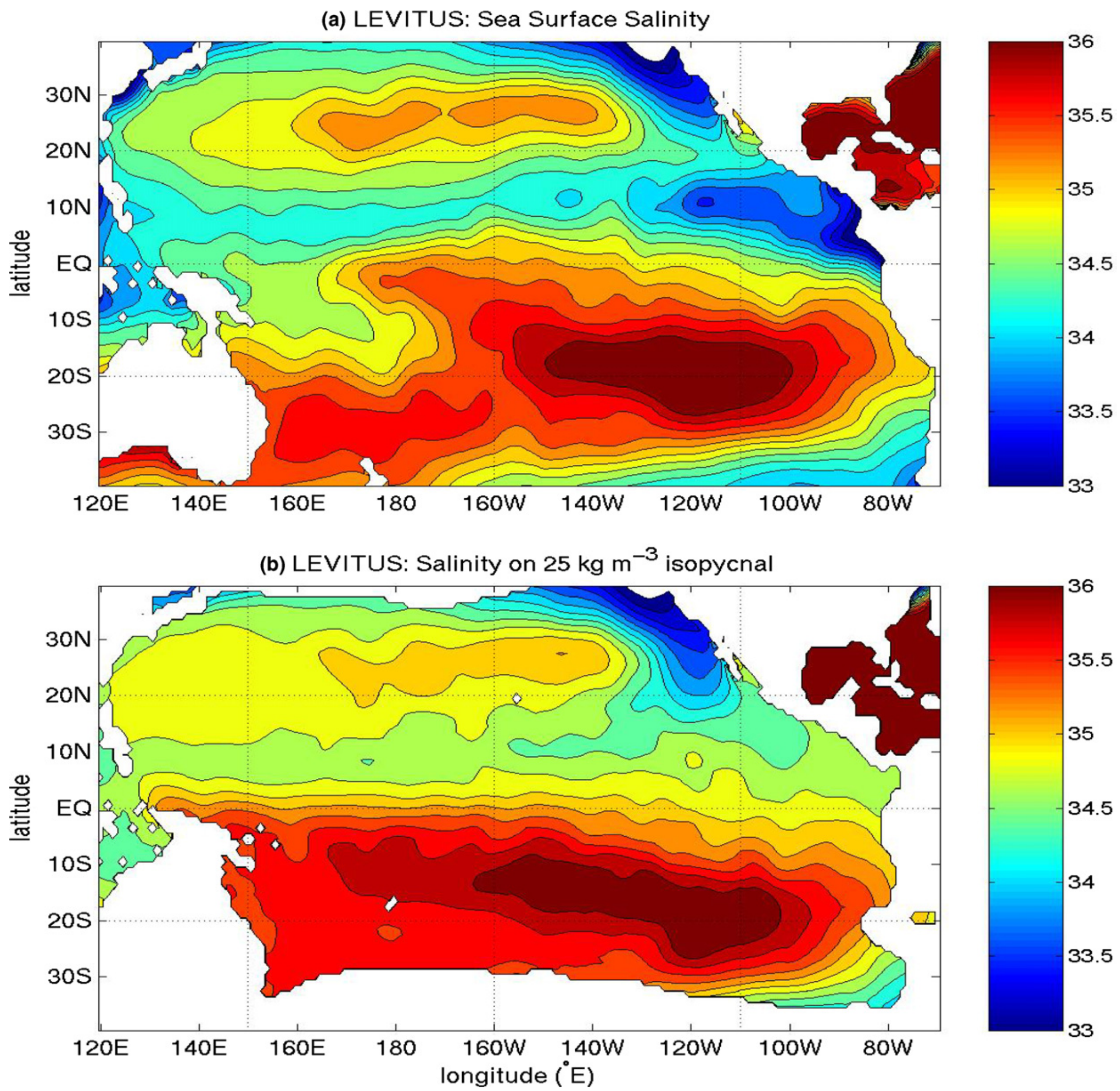

Fig. 1. Observed salinity at the ocean surface (a) and on the 25 kg m^{-3} isopycnal (b) taken from Levitus climatology, in units of psu. Contour intervals of 0.2 psu.

Regions where precipitation exceeds evaporation (E–P) are clearly denoted by areas where salinity is less than 34.8 psu (seen by comparing salinity to observed estimates of E–P, e.g., Trenberth and Guillemot (1998)). Maximum values of salinity are observed to form downwind (by approximately 5°) of the regions where E–P is a maximum; in the North Pacific between 170°E–140°W, 20°N–30°N and in two South Pacific regions between 25°S–35°S, 160°E–160°W and 15°S–25°S, 160°W–100°W.

Water with densities between 22–26 kg m^{-3} in the North Pacific and 22.5–26.2 kg m^{-3} in the South Pacific flows along isopycnal pathways to the tropical thermocline (Johnson and McPhaden, 1999; McPhaden and Zhang, 2002). Densities throughout this paper will be expressed in the standard notation (absolute density minus 1000 kg m^{-3}). The 25 kg m^{-3} isopycnal surface intersects the core of the EUC at the equator. Therefore, we plot salinity on the 25 kg m^{-3} surface to identify extratropical sources of equatorial thermocline water (Fig. 1(b)). The salinity maximum in the North Central Pacific is due to the North Pacific subtropical water that subducts into the permanent thermocline north of Hawaii and then flows west and south to the western boundary. The salinity minimum to the east of the North Pacific subtropical water is due to the fresh California Current that subducts along the eastern boundary and flows westward in the North Equatorial Current. In the South Pacific, the salinity maximum is due to the South Pacific water (12–26°S) that subducts into the permanent thermocline in a broad region centered at 20°S, 120°W. This water flows west and north to just north of the equator. Equatorial water west of 120°W has salinity greater than 35.2 psu, a direct indication that South Pacific water subducted poleward of 12°S plays a significant role in maintaining the equatorial thermocline.

2. Numerical models and observations used in this study

In this study we compare model output from NCAR's Community Climate System Model version 3 (CCSM3) to an integration of the uncoupled ocean component of the CCSM3 (POP3) with prescribed atmospheric and sea–ice forcing, as well as, to observations. The CCSM3 consists of atmosphere, land surface, ocean, and sea ice components that communicate with each other through a flux coupler. Detailed descriptions of the component models and the flux coupler can be found in Collins et al. (2006a,b), Dickinson et al. (2006), Holland et al. (2006) and Smith and Gent (2004).

The atmospheric component of the CCSM3 (The Community Atmosphere Model (CAM3), Collins et al., 2006b) is a global atmospheric general circulation model. The standard version of CAM3, which is used here, has 26 vertical levels and is based upon the Eulerian spectral dynamical core with triangular truncation at 42 and 85 wave numbers, horizontal resolutions of approximately 2.8° and 1.4°, respectively. The land surface component of the CCSM3 (The Community Land Model (CLM), Briegleb et al., 2004) uses a grid that is identical to that of CAM3.

The ocean component of the CCSM3 is an extension of the Parallel Ocean Program (POP3), documented in Danabasoglu et al. (2006), originally developed at Los Alamos National Laboratory. The ocean model configuration used in this study employs a dipole grid with a nominal horizontal resolution of 1°. The vertical dimension is treated using a depth coordinate with 40 levels extending to 5.37 km. The approximately 1-degree grid has 320 zonal points and 384 meridional points. The spacing of the grid points is 1.125° in the zonal direction and roughly 0.5° in the meridional direction with higher resolution near the equator. The sea–ice component of the CCSM3 (The Community Sea–Ice Model (CSIM), Briegleb et al., 2004) uses a grid that is identical to the ocean model grid.

POP3 is initialized in both the coupled and uncoupled models using January mean temperature and salinity fields (Levitus et al., 1998; Steele et al., 2001 in the Arctic Ocean) and a state of rest. The uncoupled POP3 simulation is forced by turbulent air–sea fluxes and wind stress calculated using atmospheric state data from the 1958–2000 global NCEP/NCAR reanalysis (Kalnay et al., 1996). This forcing is applied for three cycles, data from the last cycle of 43 years is presented in this paper. Radiative fluxes are calculated using the International Satellite Cloud Climatology Project (ISCCP) global radiative flux data products (Zhang et al., 2004). The climatological monthly mean GXGXS precipitation data set, constructed and documented by Large and Yeager (2004), is used to calculate freshwater fluxes. Under sea–ice, sea surface temperature and salinity are relaxed to observations. The details of this forcing and the resultant flux climatologies are documented in Large and Yeager (2004).

We examine model data from CCSM3 integrations B30.009 (T85) and B30.004 (T42), control runs for the anthropogenic global warming scenarios specified by the Intergovernmental Panel on Climate Change. In the control runs, radiative forcings are held fixed at 1990 levels during a 1000-year integration of the model. In these simulations, sea surface height varies locally while the ocean volume remains fixed. Therefore, the surface freshwater flux is converted into an implied salt flux using a constant reference salinity of 34.7 practical salinity units (psu). CCSM3 climatologies used in this study are calculated by averaging years 200–599 of the model integrations. Over this time period the global volume mean ocean temperature decreases by approximately 0.2 °C in both the T85 and T42 integrations and the global volume mean salinity decreases by 8.0×10^{-4} and 1.5×10^{-4} psu in the T42 and T85 integrations, respectively. Further details on climate drift in the CCSM3 control integrations are provided in Collins et al. (2006a).

In this study we compare annual mean ocean model output to salinity and temperature from the Levitus climatology (Levitus et al., 1994; Levitus and Boyer, 1994) and currents from the National Oceanic and Atmospheric Administration (NOAA) Pacific Ocean hindcast (Behringer et al., 1998). The Levitus climatology represents a synthesis of all temperature and salinity available from the National Oceanographic Data Center. These parameters have been analyzed in a consistent, objective manner at standard oceanographic analysis levels on a one-degree latitude–longitude grid. The NOAA Pacific Ocean hindcast results are derived from a model based ocean analysis system. Observed surface and subsurface ocean temperatures as well as satellite altimetry sea-level data from TOPEX/POSEIDON are assimilated into a Pacific basin ocean general circulation model starting in October 1992. The model is forced with weekly mean NOAA National Centers for Environmental Prediction operational atmospheric analyses of surface winds and heat fluxes.

3. Results

3.1. The structure of the equatorial thermocline

3.1.1. Temperature

Fig. 2 shows equatorial temperatures from the surface to 350 m from the POP3 integration (Fig. 2(a)), Levitus climatology (Fig. 2(b)), the T85 integration (Fig. 2(c)), T85 minus POP3 (Fig. 2(d)), the T42 integration (Fig. 2(e)), and T85 minus T42 (Fig. 2(f)). Below the 13 °C and above the 22 °C isotherms, POP3 is within 1 °C of the observed climatology. However, from the dateline to the eastern boundary the core and lower thermocline (approximately 15–21 °C) are greater than 1 °C too warm compared to observations. The maximum warming (3–4 °C) is centered on the POP3 20 °C isotherm. This warming results in a weakening of the modeled stratification of the thermocline. This is found to be true in both the coupled and uncoupled models. In addition, SSTs near the eastern boundary have an unrealistic local maximum.

The diffuse equatorial thermocline in both the coupled and uncoupled integrations (Fig. 2(a), (c) and (e)) indicates that this bias is due to the ocean model and not due to the coupling. Coupling does impact equatorial temperatures by causing the thermocline to become colder over the domain, seen by the greater than 2.5 °C difference near the 20 °C isotherm (Fig. 2(d)). In addition, the longitudinal extent of the Warm Pool has been reduced by approximately 20°.

The impact of an increase in resolution in the atmospheric model from T42 to T85 on the equatorial temperatures is plotted in Fig. 2(f). This figure shows that mixed layer temperatures are essentially unchanged when the resolution is increased. However, the upper thermocline in the T85 integration is warmer than in the T42 integration, with a maximum of 2 °C at the western boundary. This increase in equatorial temperatures is primarily due to the deeper Warm Pool in the T85 integration.

3.1.2. Salinity

Looking at the observed equatorial salinity field (Fig. 3(b)), the most saline water is found near the core of the thermocline with a maximum of 35.4 psu at 140°E becoming fresher to the east. The uncoupled integration (Fig. 3(a)) simulates these observed features reasonably well. However, the model is 0.1–0.2 psu more saline

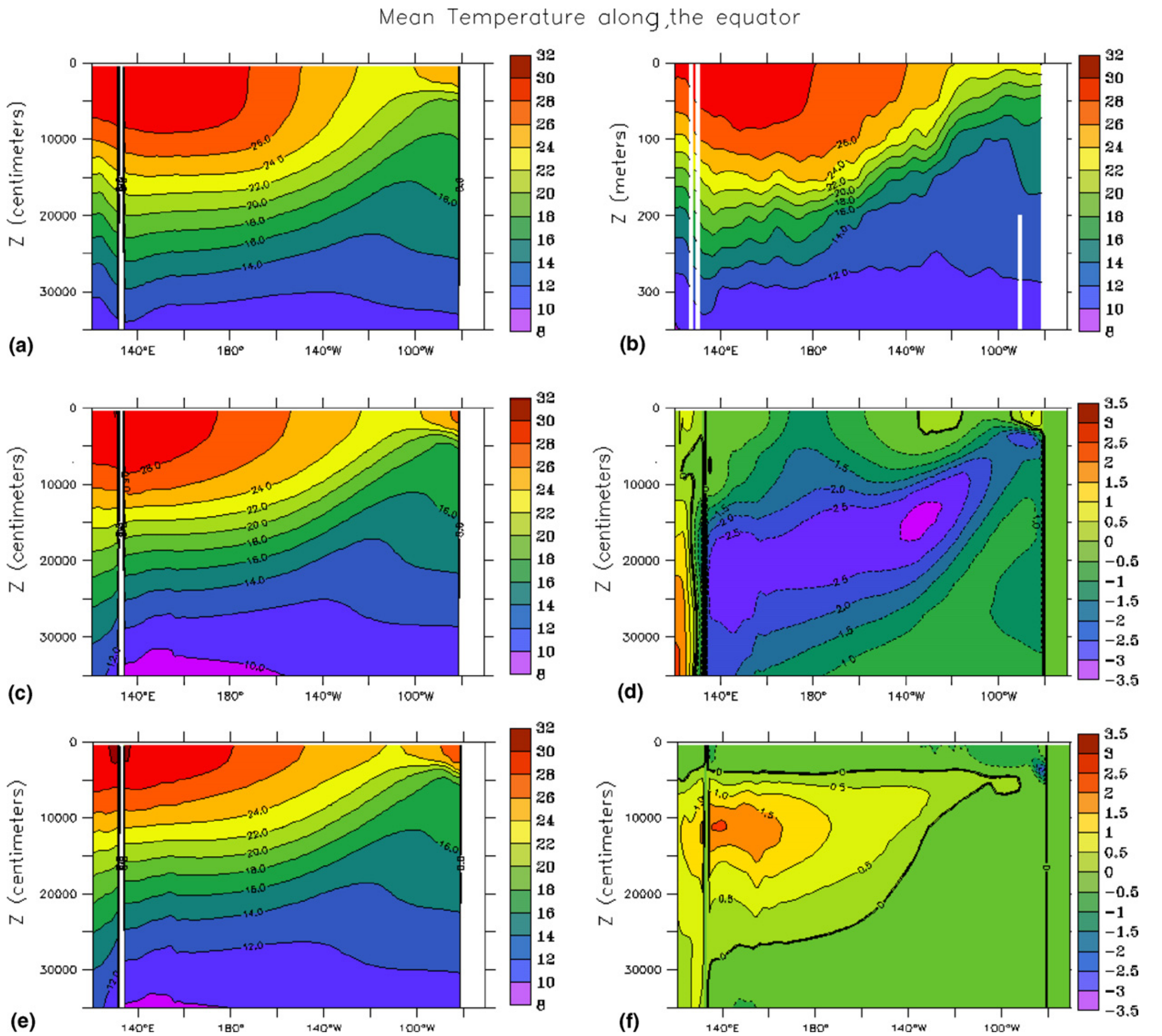

Fig. 2. Equatorial temperature to 350 m depth, in units of °C. (a) POP3, (b) NOAA Pacific, (c) T85, (d) T85–POP3, (e) T42, (f) T85–T42. Contour interval of 2 °C for (a)–(c) and (e). Contour interval of 0.5 °C for (d) and (f). Dashed contour lines indicate negative values.

than observations in the same region where the temperature is 2–4 °C greater than observations (Fig. 2), near the modeled 20 °C isotherm. The maximum in salinity in the uncoupled integration extends to the eastern boundary, potentially due to too little diapycnal mixing in the eastern Pacific. In addition, the Warm Pool is significantly fresher than observations.

The observed salinity maximum along the core of the thermocline (Fig. 3(a) and (b)) is significantly reduced in the coupled simulations. In fact, the salinity maximum seen in the core of the thermocline near the western boundary in the uncoupled integration (Fig. 3(a)) is essentially absent in the T85 integration (Fig. 3(c)). Figs. 2 and 3(d) show that the T85 integration has a colder and fresher thermocline compared to the POP3 integration. This indicates that coupling causes the water mass properties of the waters that flow from the extratropics to the equatorial thermocline to change, potentially due to a change in the temperature and salinity in the region of the 25 kg m^{-3} outcropping lines.

In the previous section it was shown that equatorial Pacific mixed layer temperatures are insensitive to the resolution of the atmospheric model (Fig. 2(f)). Fig. 3(f) shows that this is not the case with the salinity field.

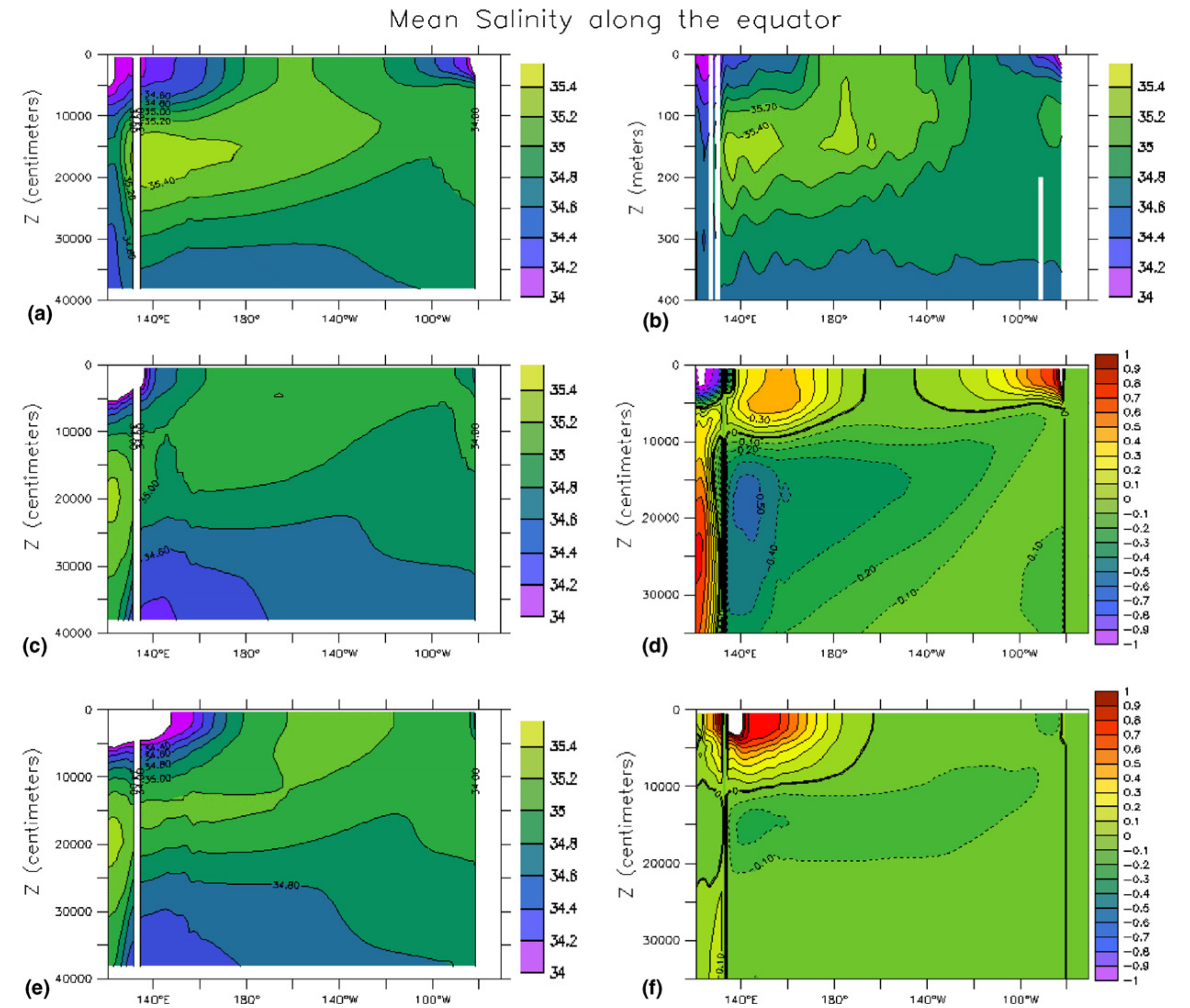

Fig. 3. Equatorial salinity to 350 m depth, in units of psu. (a) POP3, (b) NOAA Pacific, (c) T85, (d) T85–POP3, (e) T42, (f) T85–T42. Contour interval of 0.2 psu for (a)–(c) and (e). Contour interval of 0.1 psu for (d) and (f). Dashed contour lines indicate negative values.

The Warm Pool salinity increases by 0.7 psu when the resolution is increased from T42 to T85. Therefore, while the Warm Pool in the T85 simulation is too saline compared to observations (Fig. 3(d)), the Warm Pool in the T42 simulation is too fresh. This difference may be a result of the significantly larger evaporation minus precipitation (>50%) along the equator as the resolution of the atmospheric model is increased to T85 (results not shown). Interestingly, the freshening of the upper thermocline is less pronounced in the T42 integration (Fig. 3(e) and (f)).

In summary, the coupled model integrations have similar equatorial temperature structure to the uncoupled model integrations. Both the coupled and uncoupled model integrations have a more diffuse thermocline and warmer SSTs in the eastern Pacific compared to the Levitus climatology. However, the difference between the coupled and uncoupled integrations' equatorial thermocline salinity and temperature suggest that the coupling significantly changes the water mass properties of water that flows from the extratropics to the equatorial thermocline.

In the following sections we assess to what extent the differences between the coupled and uncoupled model integrations are due to variations in extratropical–tropical water mass exchange.

3.2. Zonal wind stress

Since all integrations investigated in this paper use the same ocean model, the first task is to identify how the forcing of the ocean changes when the model is run in coupled mode and when the resolution of the atmospheric model is increased. To this end we focus on changes in the zonal wind stress between the POP3, T42 and T85 integrations. In Fig. 4(a) we plot the zonal wind stress used to force the uncoupled model. In Fig. 4(b)–(d) we plot the zonal wind stress from the T85, T85 minus POP3, and T85 minus T42 integrations, respectively.

Comparing Fig. 4(a) and (b), it is seen that the T85 coupled model has zonal (westward) wind stress that is too weak between 15°S–15°N, 180–115°W and east of 115°W between 10°S–2°N (Fig. 4(c)). Poleward of this region the T85 zonal wind stress is too strong (Fig. 4(c)). This difference in the zonal wind stress increases Ekman suction equatorward of the maximum wind stress and increases Ekman pumping poleward of the maximum wind stress. The decrease in the magnitude of the equatorial zonal wind stress is consistent with the shallower Warm Pool seen in Fig. 2(c).

Fig. 4(d) plots the difference between the T85 and T42 zonal wind stress. It is seen that increasing the resolution of the atmospheric model reduces the tendency for the equatorial wind stress to be too weak and the wind stress poleward of 10°N and 10°S to be too strong. However, the anomalous trades off the coast of Central America and the weak easterlies in the central Pacific centered at 8°N and 7°S are found in both the T42 and T85 simulations. There is a poleward shift in the easterly zonal wind stress maximum in both the North and South Pacific in both the T42 and T85 simulations. Of interest to this study is the anomalous Ekman pumping forced by these winds. Since Ekman pumping is proportional to minus (plus) the meridional gradient of the zonal wind stress in the Northern (Southern) Hemisphere, negative (positive) gradients imply anomalous upwelling and positive (negative) gradients imply anomalous downwelling in the Northern (Southern) Hemisphere. Therefore, the anomalous zonal wind stress in the coupled models forces enhanced blocking of transport from the extratropics to the tropics through interior pathways and anomalous downwelling off the coast of Central America.

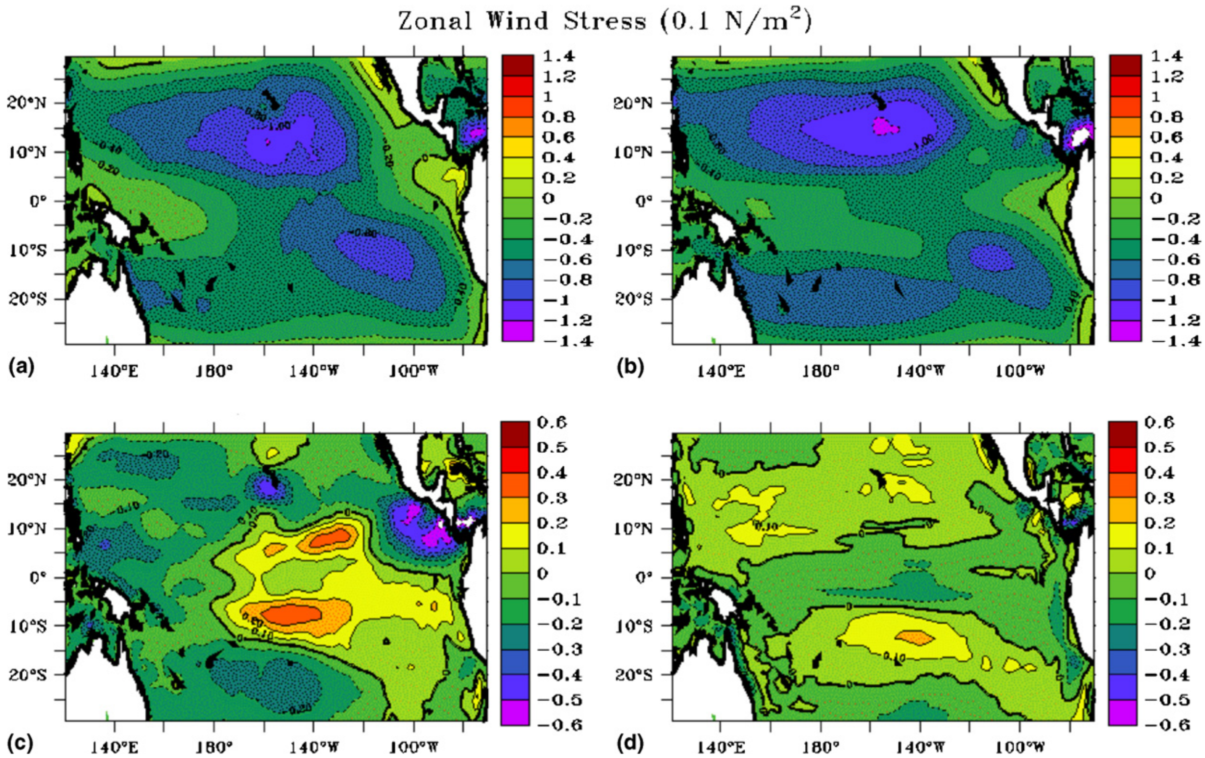

Fig. 4. Zonal wind stress, in units of N m^{-2}. (a) POP3, (b) T85, (c) T85–POP3, (d) T85–T42. Dashed contour lines indicate negative values. Contour interval of 0.2 N m^{-2} in (a) and (b). Contour interval of 0.1 N m^{-2} in (c) and (d).

3.3. Zonal currents

In the previous section we described how coupling impacts the zonal wind stress. In this section we investigate how coupling impacts the zonal currents. To this end we plot zonal surface currents and currents at 160°W as a function of latitude and depth for the three integrations and observations (NOAA Pacific hindcast currents described in Section 2), in Figs. 5 and 6, respectively. In the POP3 integration (Fig. 5(a)), the westward surface currents within 5° of the equator generally approximate the observations (Behringer et al., 1998). However, the surface countercurrents appear to be inadequately simulated. The North Equatorial Countercurrent (NECC), found north of 2°N in the west Pacific and 5°N in the east Pacific, is too weak (Figs. 5(a) and 6(a)) and does not surface in the central Pacific (e.g., Johnson, 2001). In addition, the South Equatorial

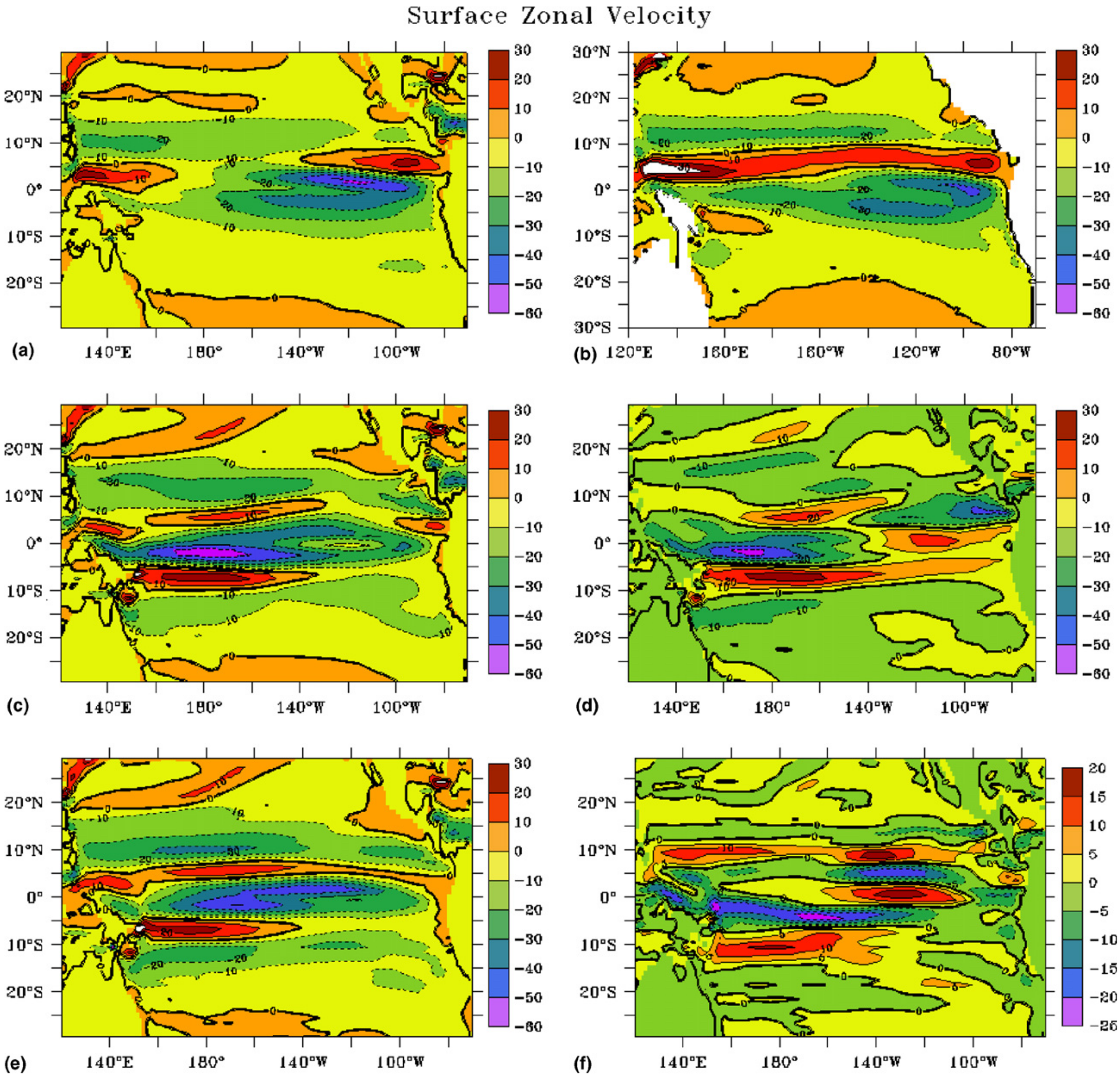

Fig. 5. Surface zonal currents, in units of cm s^{-1}. (a) POP3, (b) NOAA Pacific, (c) T85, (d) T85–POP3, (e) T42, (f) T85–T42. Contour interval of 10 cm s^{-1} for (a)–(e). Contour interval of 5 cm s^{-1} for (f). Dashed contour lines indicate negative values.

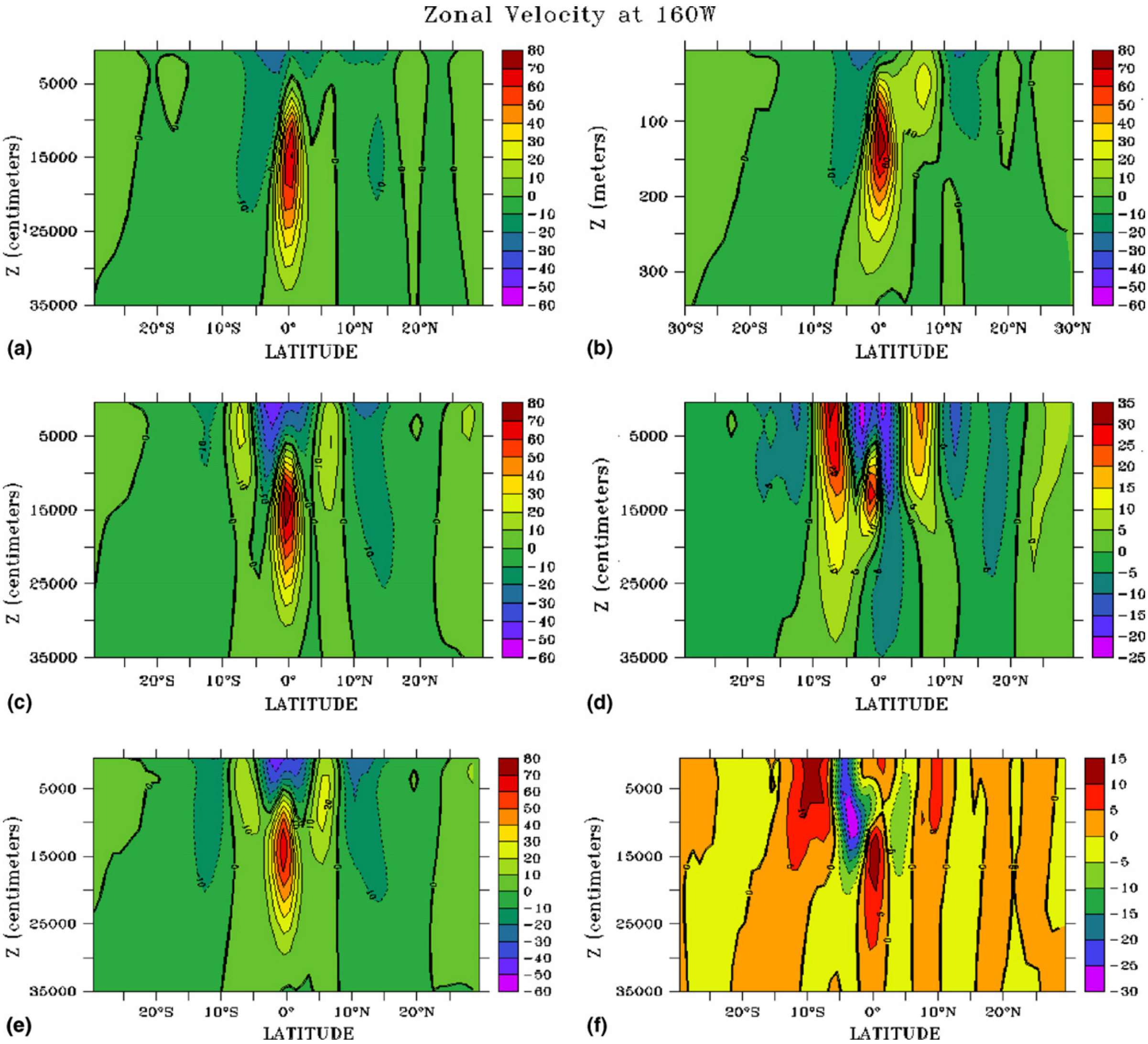

Fig. 6. Zonal currents at 160°W as a function of latitude and depth, in units of cm s^{-1}. (a) POP3, (b) NOAA Pacific, (c) T85, (d) T85–POP3, (e) T42, (f) T85–T42. Contour interval of 10 cm s^{-1} for (a)–(c) and (e). Contour interval of 5 cm s^{-1} for (d) and (f). Dashed contour lines indicate negative values.

Countercurrent (SECC), a band of weak eastward flow near 8°S caused by a wind stress minimum in the Southern Hemisphere trade winds, does not extend east of 160°W and the equatorial currents to the north of the SECC are underestimated (Figs. 5(a) and 6(a)). These biases are documented in more detail in Large and Danabasoglu (2006).

Interestingly, the coupled integrations (Fig. 5(c) and (e)) have more realistic surface countercurrents in the central North Pacific (Fig. 5(b)), the NECC extends from the western to eastern boundary as is observed. However, the maximum north of the equator near the western and eastern boundaries is underestimated. In addition, the SECC exists in both of the coupled integrations but is too strong and extends too far into the eastern Pacific compared to observations. Different from observations and the POP3 integrations, in the coupled runs the maximum equatorial zonal currents are unrealistically found in the South Pacific west of the dateline. These results can be clearly seen in the difference plots, Figs. 5(d) and 6(d). The anomalous off-equatorial currents in the coupled simulations (Fig. 5(d)) are consistent with the upwelling forced by the anomalous zonal wind stress plotted in Fig. 4(c).

Increasing the resolution from T42 to T85 increases the magnitude of the equatorial currents but does not change the general structure of the currents (Fig. 6(c), (e) and (f)).

3.4. Subduction

Water-mass properties are formed at the sea surface by air–sea interaction. After subducting into the main thermocline, water-mass properties become shielded from the atmosphere. The annual rate of subduction into the main thermocline, Sann, is evaluated as

$$\mathrm{Sann} = -w_{\mathrm{H}} - u_{\mathrm{H}} \cdot \nabla H,$$

where w_{H} and u_{H} are the vertical velocity and horizontal velocity vector at the base of the seasonal thermocline given by the maximum thickness of the winter mixed layer and ∇H is a measure of the slope of the base of the mixed layer. Since the last term in the equation for Sann is small in the Pacific (Huang and Qiu, 1994), we evaluate $\mathrm{Sann} \approx -w_{\mathrm{H}}$, i.e., the annual subduction rate can be approximated by minus the vertical velocity at the base of the wintertime mixed layer.

Fig. 7 shows the annual mean subduction, indicating where water flows from the mixed layer into the permanent thermocline when the subduction is positive and where water flows from the thermocline into the mixed layer when the subduction is negative. Focusing on subduction in the extratropics, the POP3 integration (Fig. 7(a)) shows subduction greater than approximately 40 m year^{-1} in the North Pacific extending from 170°W, 10°N to 130°W, 30°N. This is broadly consistent with the annual mean subduction estimates of Huang and Qiu (1994). In the South Pacific, subduction greater than of 40 m year^{-1} extends in an approximate 20° longitudinal band from 10°S, 145°W to 25°S, 95°W, consistent with the estimates of Huang and Qiu (1998). Subduction extends continuously from the extratropics to the tropics in the interior of the basin in both the North and South Pacific.

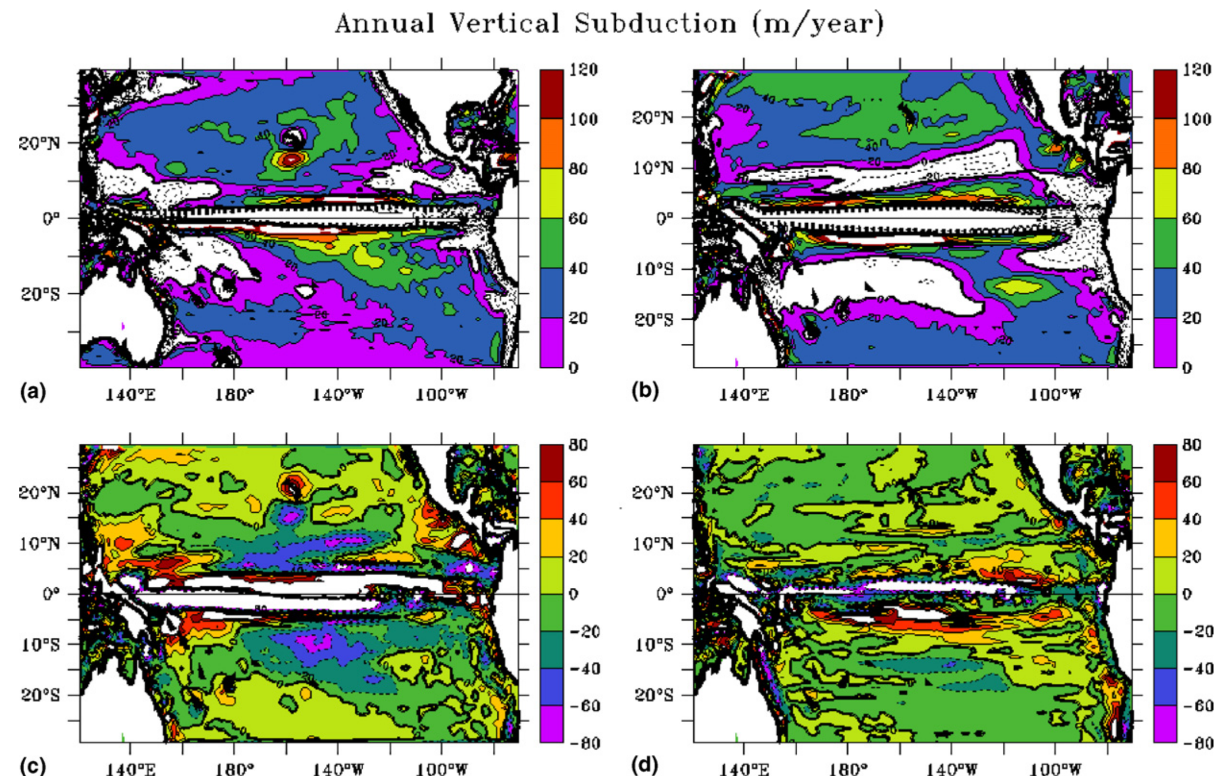

Fig. 7. Vertical subduction, in units of m year^{-1}. Contour interval of 20 m year^{-1}. Calculation described in the text. (a) POP3, (b) T85, (c) T85–POP3, (d) T85–T42. Dashed contour lines indicate negative values.

The coupled integrations (Fig. 7(b) and (d)) tend to have stronger subduction in the subtropical Pacific than the POP3 integration (seen clearly in Fig. 7(c)). In addition, both coupled integrations have anomalous regions of upwelling that extend into the central North and South Pacific near 10°N and 10°S. This upwelling is due to Ekman suction produced by the more extensive convergence zones in both the tropical North and South Pacific compared to the uncoupled integration. Following Lu and McCreary (1995), the equatorward movement of subsurface water is proportional to the Ekman pumping velocity. In regions on the poleward flanks of weakening negative Ekman pumping velocity, equatorward flowing water is diverted westward. These ''potential vorticity barriers'' cause the potential vorticity conserving flow in the subsurface branch of the STCs (e.g., Talley, 1985) to be diverted westward away from the interior.

Increasing the resolution of the atmospheric model from T42 to 85 increases the subduction biases in both the eastern subtropical North and South Pacific.

3.5. Lagrangian pathways in the upper and lower thermocline

In order to better understand the STC pathways we plot trajectories in the upper (Fig. 8) and lower equatorial thermocline (Fig. 9). The core of the EUC coincides with the 25 kg m^{-3} isopycnal in all three integrations (results not shown). Therefore, we plot the Lagrangian trajectories (calculated from annual mean data) along the 24.5 kg m^{-3} isosurface as an estimate of pathways to the upper equatorial thermocline and 25.5 kg m^{-3} isosurface as an estimate of pathways to the lower equatorial thermocline. The upper (lower) plot in both figures shows the trajectories for the POP3 (T85) integration. The triangles indicate intervals of one year. The Lagrangian floats are released at 20°N and 20°S. Black lines indicate pathways to the interior. Blue lines indicate pathways to the equator through the western boundary. Red lines indicate trajectories that recirculate back to the subtropical Pacific. Looking at Fig. 8, coupling essentially elongates the pathways that flow through the interior to the equator (due to the larger PV barrier in the North Pacific in the coupled

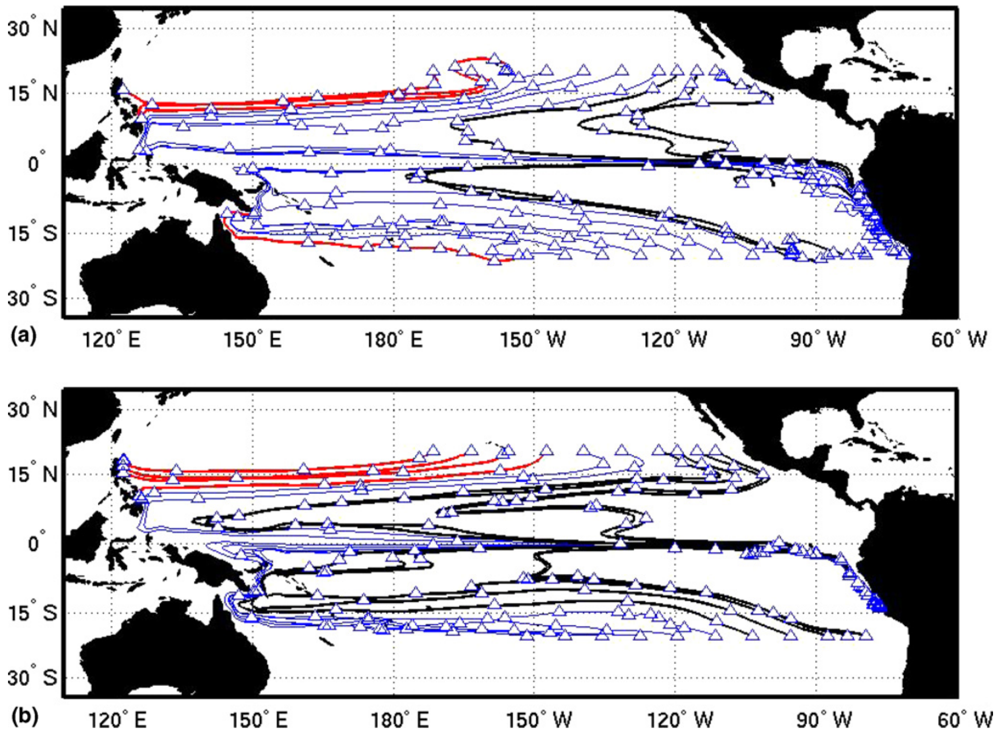

Fig. 8. Lagrangian trajectories along 24.5 kg m^{-3} isopycnal surfaces. Trajectories are initiated along 20°N and 20°S. Red lines indicate trajectories that flow poleward along the western boundary. Blue lines indicate trajectories that reach the equator through the western boundary. Black lines indicate interior pathways. (a) POP3, (b) T85.

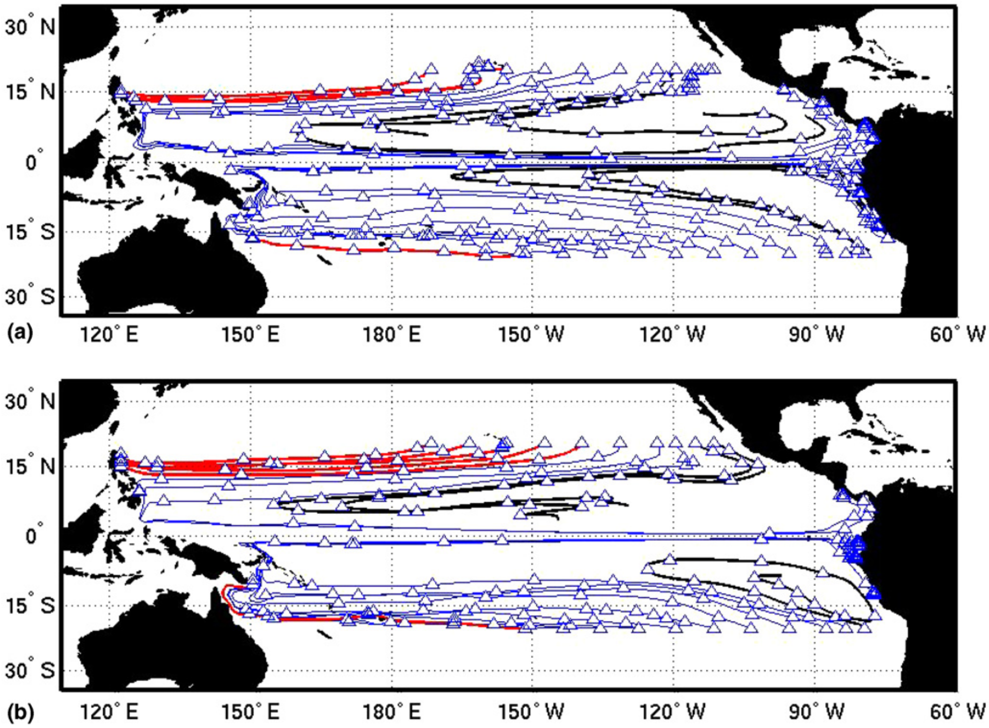

Fig. 9. Lagrangian trajectories along 25.5 kg m^{-3} isopycnal surfaces. Trajectories are initiated along 20°N and 20°S. Red lines indicate trajectories that flow poleward along the western boundary. Blue lines indicate trajectories that reach the equator through the western boundary. Black lines indicate interior pathways. (a) POP3, (b) T85.

integrations) but otherwise has little impact. However, in the South Pacific there are significant differences between the coupled and uncoupled integrations. In the POP3 integrations, pathways flow to the western boundary to within 5° of the equator. By contrast in the coupled integration, pathways that flow to the western boundary equatorward of 15°S are redirected to the interior by the unrealistically large SECC.

Comparing Fig. 8(a) with Fig. 9(a), it appears that in the North Pacific interior pathways to the lower thermocline come within a few degrees of the equator and recirculates within the tropical North Pacific without upwelling at the equator. The most significant difference between pathways in the South Pacific is that interior pathways to the upper equatorial thermocline originate from the eastern boundary to 100°W while interior pathways to the lower equatorial thermocline originate in a more limited region near the eastern boundary.

Comparing the pathways to the lower equatorial thermocline in the POP3 and T85 integrations (Fig. 9(a) and (b)) it is seen that interior pathways in both the North and South Pacific in the T85 integration do not reach the equator. Only water that flows through the western boundary pathways contributes to the EUC in the T85 integration. In addition, in the North Pacific only water subducted in a limited window between 135°W and 120°W flows to the western boundary (compared to 160–120°W in the POP3 integration).

3.6. Salinity

In this section we identify the regions where air–sea interaction forces the water mass properties of the water that subducts into the permanent thermocline and flows to the equator. Following the work of Tsuchiya (1981, 1999), among others, we use salinity as a tracer for water that subducts in the extratropics and flows to the equator along pycnocline pathways. To this end we plot salinity at the sea surface (SSS) and on the 25 kg m^{-3} isopycnal (the density of the core of the EUC and water that is denser than the extratropical mixed layer, i.e., in the permanent thermocline, for all three integrations) for the POP3 (Fig. 10(a) and (b)), T85 (Fig. 10(c) and (d)), and T42 (Fig. 10(e) and (f)) integrations. On the 25 kg m^{-3} isopycnal surface large-scale

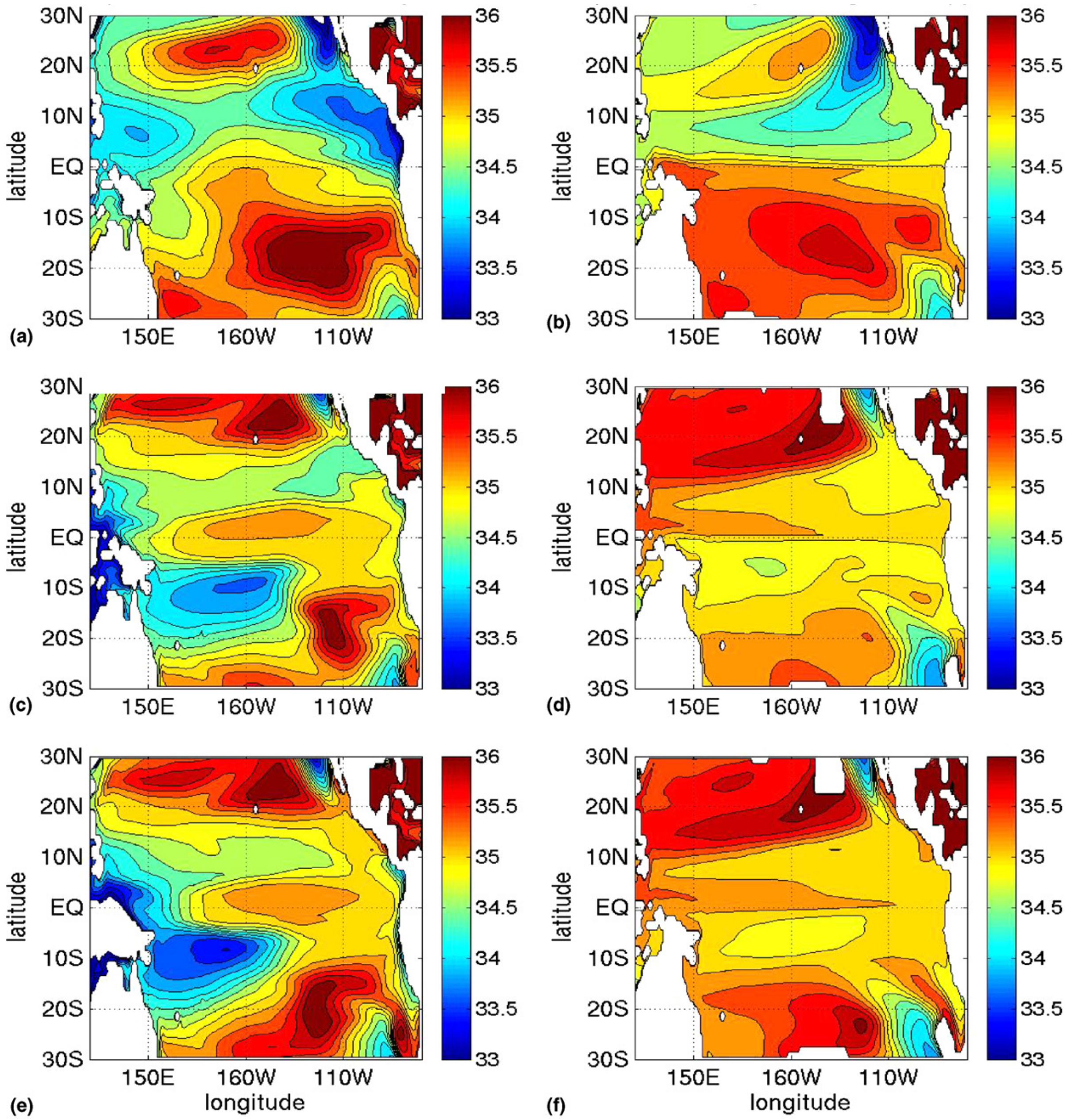

Fig. 10. Salinity on the 25 kg m^{-3} isopycnal and at the ocean surface, in units of psu. (a and b) POP3, (c and d) T85, (e and f) T42. Contour intervals of 0.2 psu.

potential vorticity contours coincide with salinity contours (results not shown), indicating that potential vorticity is essentially conserved in the subsurface equatorward branches of the STCs.

The POP3 SSS (Fig. 10(a)) simulates observed SSS well (Fig. 1(a)), except that the region of maximum salinity north of Hawaii is too saline by approximately 0.6 psu. In the North Pacific, the maximum SSS northwest of Hawaii (Fig. 10(a)) is seen to subduct in that region into the permanent thermocline (Fig. 10(b)) and then travel westward to the western boundary. Due to the dominance of more saline water from the South Pacific, it is not possible to determine if this water flows to the equator. The fresh water formed along the northeastern boundary also subducts into the permanent thermocline and travels to within a few degrees of the equator. In the South Pacific, the water formed near 140°W and 20°S subducts into the permanent thermocline and flows to the equator through western boundary and interior pathways. This water of South Pacific origin reaches and crosses the equator. Therefore, in the POP3 integration the water that primarily maintains the EUC comes from the South Pacific, consistent with observation (Fig. 1(b)). This water is significantly warmer and saltier than water that flows to the equator from the North Pacific.

Looking at Fig. 10(c), the SSS in the T85 integration is significantly different from the SSS in the POP3 integration (Fig. 10(a)). The salinity maximum in the North Pacific extends from the western boundary to 120°W, with a maximum of 36 psu east of Hawaii. The fresh water in the California Current along the eastern boundary does not extend south of 20°N. In addition, there is a region of minimum salinity in the region of the ITCZ but the salinity is almost 1 psu larger than in the POP3 integration. Most striking in the South Pacific is the region of fresh water with a minimum salinity of 33.6 psu that extends along 10°S. This fresh water bias is due to errors in the mean precipitation (Large and Danabasoglu, 2006). This region of anomalously strong precipitation limits the region where evaporation exceeds precipitation to west of 120°W.

In the T85 simulation in the North Pacific, water subducts into the permanent thermocline to the north of Hawaii and flows southwest to the western boundary (Fig. 10(d)), similar to the POP3 integration. The water that subducts in this region is significantly more saline (>0.8 psu) than water that subducts in this region in observations (Fig. 1(b)) and the POP3 simulation (Fig. 10(b)). After reaching the equatorial region, this water flows just north of the equator to the central equatorial Pacific. Different from observations and the POP3 simulation, this North Pacific water is more saline than water that reaches the equatorial region from the South Pacific. In addition, the water that subducts from the California Current is significantly more saline (>1 psu) than in observations and the POP3 simulation.

In the South Pacific, water that subducts in the subtropical east South Pacific flows directly to the western boundary. This water then flows along the western boundary to the equator. There is no indication that water flows directly to the equator through interior pathways in the lower thermocline in the coupled simulations. Water that subducts near 20°S, 120°W is ~0.5 psu fresher than in the POP3 simulation, causing water that flows to the equator from the South Pacific to be fresher than water that flows to the equator from the North Pacific. Interestingly, the water that subducts at 20°S, 120°W is approximately 1 °C colder, resulting in little change in the 25 kg m^{-3} outcropping lines (results not shown). Water at the equator has the same salinity as water that flows along the western boundary in the South Pacific. This indicates that, in the coupled model as in observations, the water mass properties in the equatorial thermocline are determined by water that flows from the subtropical South Pacific.

Comparing Fig. 10(c) and (e), it is seen that increasing the resolution from T42 to T85 results in fresher water in the region of the ITCZ and more saline water in the region of the SPCZ and on the equator near the western boundary, bringing the SSS distribution closer to the uncoupled POP3 simulation (Fig. 10(a)). However, looking at Fig. 3(f), this change in SSS in the Warm Pool region overcompensates for the fresh bias in the T42 simulation by making the Warm Pool too saline. Comparing Fig. 10(d) with Fig. 10(f) indicates that the most significant impact of an increase in the resolution of the atmospheric model on equatorward pycnocline flow is a better defined ITCZ in the eastern North Pacific, and therefore a better defined potential vorticity barrier that blocks the flow of water to the equator through interior pathways.

3.7. Meridional transports

McPhaden and Zhang (2002) estimate subtropical water that flows to the equatorial thermocline as transport in density classes between 22 and 26 kg m^{-3} at 9°N and 22.5–26.2 kg m^{-3} at 9°S. In Table 2 we list the meridional equatorward pycnocline transports within the western boundary currents and the basin interior separately at 9°N and 9°S, as well as, the net convergence within the western boundary and the basin interior. Transports are calculated at these latitudes in order to directly compare the transport in the models to the observed transports of McPhaden and Zhang (2002). However, water that flows poleward in the surface branch of the STCs has densities up to 23.5 kg m^{-3} in the eastern tropical Pacific (results not shown). Therefore, we include only equatorward transport within these density classes in the totals. It is important to note that (looking at Figs. 8 and 9) interior transport at 9°N or 9°S does not mean that this water necessary flows to the equator through the basin interior. Transports at these latitudes can still either flow to the western boundary (Fig. 8(a)) or recirculate within the tropics without reaching the equator (Fig. 9(b)).

Table 2
Model pycnocline transports divided into interior and western boundary transports in the North and South Pacific, as well as, net (South Pacific minus North Pacific) interior and western boundary convergence

	Interior pycnocline transport 9°N	Western boundary transport 9°N	Interior pycnocline transport 9°S	Western boundary transport 9°S	Interior pycnocline convergence	Western boundary convergence
POP3	−12.2 Sv	−6.6 Sv	18.5 Sv	6.8 Sv	30.7 Sv	13.3 Sv
T85	−9.8 Sv	−8.0 Sv	7.5 Sv	14.0 Sv	17.3 Sv	22.0 Sv
T42	−8.7 Sv	−8.4 Sv	4.2 Sv	18.0 Sv	12.8 Sv	26.4 Sv

Density ranges used in the calculations are described in the text. Transport is in units of Sv.

Comparing the transport for the POP3 integration to observed transports (Table 1), the total convergence is consistent with observations. However, there is significantly more transport in the interior and less transport in the western boundary than observed. This is the case for transports in both the North and South Pacific. This overestimated interior transport in the North Pacific is partly due to water that originates in the California Current that flows south and west to within a few degrees of the equator (Fig. 10(b)). Looking at Fig. 1(a), in observations the low salinity water that subducts in the northeast Pacific does not flow equatorward of the salinity minimum formed by the ITCZ.

The net western boundary and interior pycnocline transport convergences for the coupled integrations are more consistent with observed transports calculated by McPhaden and Zhang (2002) than the POP3 integration. However, the coupled integrations have approximately 5 Sv ($1\ \text{Sv} \equiv 10^6\ \text{m}^3\ \text{s}^{-1}$) less pycnocline convergence between 9°N and 9°S than the POP3 integration (∼4 Sv from the South Pacific and ∼1 Sv from the North Pacific). This reduction in transport is consistent with the ∼10% larger zonally integrated westward zonal wind stress at 9°N and 9°S in the POP3 integration compared to the T85 integration (results not shown). This reduction in transport is due to a decrease in transport from the South Pacific, primarily through interior pathways. This result indicates that even though there is more subduction in the subtropical North Pacific in the T85 simulation (Fig. 7(c)) the narrower window of longitudes where pathways lead to the equator, seen in the Lagrangian trajectories Figs. 8 and 9, causes a net decrease in equatorward transport from the North Pacific.

The T42 integration appears to have too little transport along interior pathways and too much transport along western boundary pathways in the South Pacific. However, these deficits are less apparent when the resolution of the atmospheric model is increased to T85.

4. Summary and discussion

In this study we compared the simulation of the climate mean STCs in the CCSM3 (with both a T42 and T85 atmospheric component) to observations and to an uncoupled POP3 simulation. Since the STCs provide water that maintains the equatorial thermocline, we first documented the biases in the equatorial temperature and salinity fields. It was shown that the uncoupled POP3 simulation had equatorial temperatures within 1 °C of observations expect for a more diffuse thermocline with a warming of 2–4 °C centered on the 20 °C isotherm east of the dateline. The thermocline in the coupled simulations was shown to be too cold and fresh compared to the observations and the uncoupled POP3 simulation. The T42 simulation had a Warm Pool that was too fresh compared to the POP3 simulation, while the T85 simulation was too saline.

We then investigate to what extent these biases in the equatorial temperature and salinity fields were due to the simulation of extratropical–tropical water mass exchanges in the coupled models. We demonstrated that the zonally integrated transport convergence at the equator in the subsurface branch of the climate mean STCs was well simulated in the uncoupled ocean model, even though there is more transport in the interior than observed due to the weak NECC and SECC in the ocean model. The coupled models' cold and fresh bias in the equatorial thermocline was then shown be due to the subduction of significantly fresher and colder water in the South Pacific. This freshening is due to too much precipitation in the South Pacific Convergence Zone. Even though more saline water subducts in the North Pacific and flows to the tropics, this water does not dominate at the equator.

Lagrangian trajectories of water that flows to the equatorial thermocline were calculated to demonstrate that the anomalously large potential vorticity barriers in the coupled simulations in both the North and South Pacific prevented water in the lower thermocline from reaching the equator. Salinity on 25 kg m^{-3} isopycnals and Lagrangian trajectories indicate that the equatorial thermocline is primarily maintained by water that subducts in the subtropical South Pacific in both the coupled and uncoupled simulations.

Coupling reduced the net equatorward pycnocline transport, by ~4 Sv at 9°S and ~1 Sv at 9°N, primarily by limiting the longitudinal window where water that subducts in the subtropics flows to the equatorial pycnocline. Interestingly, this net decrease in equatorial pycnocline convergence did not create a warm bias in the equatorial SSTs, potentially due to the significantly colder water in the equatorial thermocline that upwells in the eastern equatorial Pacific.

An increase in the atmospheric resolution from T42 to T85 resulted in more realistic equatorial trades and off-equatorial convergence zones. However, the change in equatorial precipitation was shown to change the fresh bias in the T42 simulation to a saline bias in the T85 simulation.

In this study, we have delineated some of the factors that cause coupling between the ocean and the atmosphere to alter the structure and strength of the Pacific STCs in the model. We are in the process of investigating to what extent this change in the climate mean STCs impacts the climate variability of the coupled system, specifically, interannual tropical Pacific variability and the response of the Pacific basin to an increase in Greenhouse gases.

Acknowledgments

The authors thank Peter Gent, Dongxiao Zhang and two reviewers for their feedback on this work. We thank the Oceanography and Climate Modeling Divisions at the National Center for Atmospheric Research for providing the model output analyzed in this study. A.S. acknowledges the support of the NOAA Climate Program Office and the Office of Global Programs as a Climate Model Evaluation Project (CMEP) under the US CLIVAR Program. I.W. acknowledges the support of Grants FAPESP-00/02958-7, CNPq 300223/935, CNPq 300561/91-1 and CNPq 300040/94-6.

References

Behringer, D.W., Ji, M., Leetmaa, A., 1998. An Improved coupled model for ENSO prediction and implications for ocean initialization. Part I: The ocean data assimilation system. Mon. Weather Rev. 126, 1013–1021.

Briegleb, B.P., Bitz, C.M., Hunke, E.C., Lipscomb, W.H., Holland, M.M., Schramm, J.L., Moritz, R.E., 2004. Scientific description of the sea ice component in the Community Climate System Model, Version Three. Technical Report NCAR/TN-463+STR, National Center for Atmospheric Research, Boulder, CO 80307-3000, pp. 78.

Butt, J., Lindstrom, E., 1994. Currents off the east coast of New Ireland, Papua New Guinea, and their relevance to regional undercurrents in the Western Equatorial Pacific Ocean. J. Geophys. Res. 99 (C6), 12503–12514.

Collins, W.D., Bitz, C.M., Blackmon, M.L., Bonan, G.B., Bretherton, C.S., Carton, J.A., Chang, P., Doney, S.C., Hack, J.J., Henderson, T.B., Kiehl, J.T., Large, W.G., McKenna, D.S., Santer, B.D., Smith, R.D., 2006a. The Community Climate System Model, Version 3. J. Climate 19, 2122–2143.

Collins, W.D., Rasch, P.J., Boville, B.A., Hack, J.J., McCaa, J.R., Williamson, D.L., Briegleb, B., Bitz, C., Lin, S.-J., Zhang, M., 2006b. The Formulation and Atmospheric Simulation of the Community Atmosphere Model: CAM3. J. Climate 19, 2144–2161.

Danabasoglu, G., Large, W.G., Tribbia, J.J., Gent, P.R., Briegleb, B.P., McWilliams, J.C., 2006. Diurnal ocean–atmosphere coupling. J. Climate 19, 2347–2365.

Dickinson, R.E., Oleson, K.W., Bonan, G.B., Hoffman, F., Thornton, P., Vertenstein, M., Yang, Z.-L., Zeng, X., 2006. The Community Land Model and Its Climate Statistics as a Component of the Community Climate System Model. J. Climate 19 (11).

Fine, R., Reid, J.L., Ostlund, H.G., 1981. Circulation of tritium n the Pacific Ocean. J. Phys. Oceanogr. 11, 3–14.

Fine, R., Peterson, W.H., Ostlund, H.G., 1987. The penetration of tritium into the tropical Pacific. J. Phys. Oceanogr. 17, 553–564.

Gu, D., Philander, S.G.H., 1997. Interdecadal climate fluctuations that depend on exchanges between the tropics and the extratropics. Science 275, 805–807.

Holland, M.M., Bitz, C.M., Hunke, E.C., Lipscomb, W.H., Schramm, J.L., 2006. Influence of the sea ice thickness distribution on polar climate in CCSM3. J. Climate 19, 2398–2414.

Huang, B., Liu, Z., 1999. Pacific subtropical-tropical thermocline water exchange in the National Centers for Environmental Prediction ocean model. J. Geophys. Res. 104, 11065–11076.

Huang, R.X., Qiu, B., 1994. Three-dimensional structure of the wind driven circulation in the subtropical North Pacific. J. Phys. Oceanogr. 24, 1608–1622.

Huang, R.X., Qiu, B., 1998. The structure of the wind-driven circulation in the subtropical South Pacific Ocean. J. Phys. Oceanogr. 28, 1173–1186.

Johnson, G.C., 2001. The Pacific Ocean subtropical cell surface limb. Geophys. Res. Lett. 28, 1771–1774.

Johnson, G.C., McPhaden, M.J., 1999. Interior pycnocline flow from the subtropical to the equatorial Pacific Ocean. J. Phys. Oceanogr. 29, 3073–3089.

Kalnay, E., Kanamitsu, M., Kistler, R., Collins, W., Deaven, D., Gandin, L., Iredell, M., Saha, S., White, G., Woollen, J., Zhu, Y., Chelliah, M., Ebisuzaki, W., Higgins, W., Janowiak, J., Mo, K., Ropelewski, C., Leetmaa, A., Reynolds, R., Jenne, R., 1996. The NCEP/NCAR 40-year reanalysis project. Bull. Am. Met. Soc. 77, 437–471.

Kleeman, R., McCreary, J.P., Klinger, B.A., 1999. A mechanism for the decadal variation of ENSO. Geophys. Res. Lett. 26, 743–747.

Large, W.G., Danabasoglu, G., 2006. Attribution and impacts of upper ocean biases in CCSM3. J. Climate 19 (11).

Large, W.G., Yeager, S.G., 2004. Diurnal to decadal global forcing for ocean and sea–ice models: the data sets and flux climatologies. NCAR Technical Note NCAR/TN-460+STR, pp. 111.

Levitus, S., Boyer, T.P., 1994. World Ocean Atlas 1994: Temperature. NOAA Atlas NESDIS 4. US Department of Commerce, Washington, DC, vol. 4, pp. 117.

Levitus, S., Burgett, R., Boyer, T.P., 1994. World Ocean Atlas 1994: Salinity. NOAA Atlas NESDIS 3. US Department of Commerce, Washington, DC, vol. 3, pp. 99.

Levitus, S., Boyer, T., Conkright, M., Johnson, D., O'Brien, T., Antonov, J., Stephens, C., Gelfeld, R., 1998. World Ocean Database 1998: Introduction. NOAA Atlas NESDIS 18. US Government Printing Office, Washington, DC, vol. 1, pp. 346.

Lindstrom, E., Lukas, R., Fine, R., Firing, E., Godfrey, S., Meyers, G., Tsuchiya, M., 1987. The western equatorial Pacific Ocean circulation study. Nature 330, 533–537.

Liu, Z., Huang, B., 1998. Why is there a tritium maximum in the central equatorial Pacific thermocline? J. Phys. Oceanogr. 28, 1527–1533.

Liu, Z., Philander, S.G.H., Pakanowski, R.C., 1994. A GCM study of tropical–extratropical upper ocean water exchange. J. Phys. Oceanogr. 24, 2606–2623.

Lu, P., McCreary, J.P., 1995. Influence of the ITCZ on the flow of thermocline water from the subtropical to the equatorial Pacific Ocean. J. Phys. Oceanogr. 25, 3076–3088.

Lu, P., McCreary, J.P., Klinger, B., 1998. Meridional circulation cells and the source waters of the Pacific equatorial undercurrent. J. Phys. Oceanogr. 28, 62–84.

McCreary, J., Lu, P., 1994. On the interaction between the subtropical and the equatorial oceans: The subtropical cell. J. Phys. Oceanogr. 24, 466–497.

McPhaden, M.J., Zhang, D., 2002. Slowdown of the meridional overturning circulation in the upper Pacific Ocean. Nature 415, 603–608.

Smith, R., Gent, P., 2004. Reference manual for the Parallel Ocean Program (POP) ocean component of the Community Climate System Model (CCSM2.0 and 3.0), Technical Report LAUR-02-2484, LANL, pp. 75.

Steele, M., Morley, R., Ermold, W., 2001. PHC: a global ocean hydrography with a high quality Arctic Ocean. J. Climate 14, 2079–2087.

Talley, L.D., 1985. Ventilation of the subtropical North Pacific: the shallow salinity minimum. J. Phys. Oceanogr. 15, 633–649.

Trenberth, K.E., Guillemot, C.J., 1998. Evaluation of the atmospheric moisture and hydrological cycle in the NCEP/NCAR reanalyses. Climate Dyn. 14, 213–231.

Tsuchiya, M., 1981. The origin of the Pacific equatorial 13 °C water. J. Phys. Oceanogr. 11, 794–812.

Wyrtki, K., Kilonsky, B., 1984. Mean water and current structure during the Hawaii-to-Tahiti shuttle experiment. J. Phys. Oceanogr. 14, 242–254.

Zhang, Y., Rossow, W.B., Lacis, A.A., Oinas, V., Mishchenko, M.I., 2004. Calculation of radiative fluxes from the surface to top of atmosphere based on ISCCP and other global data sets: refinements of the radiative transfer model and the input data. J. Geophys. Res., 109. doi:10.1029/2003JD004457.